1-31-2004

Multivariate Analysis of Cross-Hole Georadar Velocity and Attenuation Tomograms for Aquifer Zonation

Jens Tronicke
ETH-Hönggerberg

Klaus Holliger
ETH-Hönggerberg

Warren Barrash
Boise State University

Michael D. Knoll
Boise State University

 DOI: 10.1029/2003WR002031

Multivariate analysis of cross-hole georadar velocity and attenuation tomograms for aquifer zonation

Jens Tronicke and Klaus Holliger

Swiss Federal Institute of Technology, Institute of Geophysics, ETH-Hönggerberg, Zürich, Switzerland

Warren Barrash and Michael D. Knoll

Center for Geophysical Investigation of the Shallow Subsurface (CGISS), Boise State University, Boise, Idaho, USA

Received 3 February 2003; revised 7 November 2003; accepted 18 November 2003; published 31 January 2004.

[1] We have investigated the potential of combining cross-hole georadar velocity and attenuation tomography as a method for characterizing heterogeneous alluvial aquifers. A multivariate statistical technique, known as *k*-means cluster analysis, is used to correlate and integrate information contained in velocity and attenuation tomograms. Cluster analysis allows us to identify objectively the major common trends in the tomographic data and thus to "reduce" the information to a limited number of characteristic parameter combinations. The application of this procedure to two synthetic data sets indicates that it is a powerful tool for converting the complex relationships between the tomographically derived velocity and attenuation structures into a lithologically and hydrologically meaningful zonation of the probed region. In addition, these synthetic examples allow us to evaluate the reliability of further petrophysical parameter estimates. We find that although absolute values of the tomographically inferred petrophysical parameters often differ significantly from the actual parameters, the clustering approach enables us to reliably identify the major trends in the petrophysical properties. Finally, we have applied the approach to a cross-hole georadar data set collected in a well-studied alluvial aquifer. A comparison of the clustered tomographic section with well-log data demonstrates that our approach delineates the hydrostratigraphic zonation. *INDEX TERMS:* 0915 Exploration Geophysics: Downhole methods; 1829 Hydrology: Groundwater hydrology; 5109 Physical Properties of Rocks: Magnetic and electrical properties; *KEYWORDS:* aquifer zone, cross-hole tomography, ground-penetrating radar, multivariate statistics, unconfined aquifers

Citation: Tronicke, J., K. Holliger, W. Barrash, and M. D. Knoll (2004), Multivariate analysis of cross-hole georadar velocity and attenuation tomograms for aquifer zonation, *Water Resour. Res.*, *40*, W01519, doi:10.1029/2003WR002031.

1. Introduction

[2] Knowledge of the distribution of hydrological parameters is a prerequisite for reliable predictions of groundwater flow and contaminant transport. Traditionally, the hydrological properties of aquifers are constrained by drilling (e.g., core analysis, geophysical logging) and/or tracer and pumping experiments. Borehole studies provide locally detailed information, but are inherently 1-D in nature, whereas commonly applied tracer and pumping tests tend to capture averaged properties of the probed region. Without complementary information, these traditional techniques are generally inadequate for reliably characterizing laterally heterogeneous alluvial aquifers [e.g., *Sudicky*, 1986]. There is, however, widespread evidence that spatial variations of hydrological parameters tend to be closely correlated with lithological changes [*Anderson*, 1989; *Jussel et al.*, 1994; *Klingbeil et al.*, 1999]. This offers the prospect of mapping pertinent lithological and hydrological zonations of alluvial aquifers with modern geophysical techniques [e.g., *Rubin et al.*, 1992; *Hyndman and Gorelick*, 1996; *Hyndman et al.*, 2000].

0043-1397/04/2003WR002031$09.00

[3] In electrically resistive materials, ground-penetrating radar (georadar) can provide the highest resolution of any geophysical technique. A number of surface and cross-hole georadar surveys have shown the potential of this geophysical tool for characterizing shallow aquifers [*Beres and Haeni*, 1991; *Young and Sun*, 1996; *Tronicke et al.*, 1999; *Hubbard et al.*, 2001], the vadose zone [*Hubbard et al.*, 1997; *Binley et al.*, 2001], and exposed aquifer analogs [*Asprion and Aigner*, 1999; *Corbeanu et al.*, 2001; *Tronicke et al.*, 2002a]. Cross-hole georadar tomography in particular seems to have great potential for complementing and enhancing hydrological data obtained with more traditional techniques. For example, *Hubbard et al.* [2001] found cross-hole tomographic georadar data highly useful to assist the development of a hydrogeological model for the sandy aquifer at the South Oyster Bacterial Transport Site near Oyster, Virginia. In other recent studies, *Binley et al.* [2001] successfully applied the technique to map temporal changes of the moisture content in the vadose zone, and *Goldstein et al.* [2003] mapped changes in a conductive tracer plume during its passage through cross-hole planes in the shallow alluvial aquifer at the Boise Hydrogeophysical Research Site near Boise, Idaho. In such monitoring studies, a tomographic image of the site before or at the beginning

of the experiment is used as a reference and relative changes with respect to this reference image are mapped. In the georadar regime of electromagnetism, wave velocity is mostly governed by the dielectric permittivity, which in turn depends strongly on water content and thus, for saturated materials, on the porosity of the probed soils and rocks [*Davis and Annan*, 1989; *Greaves et al.*, 1996]. Attenuation of georadar waves is largely controlled by the electrical conductivity of the subsurface, which may, for example, be indicative of the clay content or of the conductivity of the pore water [*Davis and Annan*, 1989]. We suggest that a combined interpretation of cross-hole georadar velocity and attenuation tomograms may be a useful means of characterizing alluvial aquifers. Although interest in this approach is increasing [e.g., *Hubbard et al.*, 2001; *Chen et al.*, 2001; *Tronicke et al.*, 2002b], its potential remains largely untapped. A major reason for this lies in the inherent difficulty of translating the generally complex and seemingly chaotic relationship between velocity and attenuation tomograms into hydrologically meaningful, zoned subsurface models. In this study, we explore the potential of a multivariate statistical technique known as cluster analysis as a means of addressing this problem in a systematic and objective fashion. We first test the validity of this approach on two synthetic data sets and then apply it to a cross-hole georadar data set acquired at a well-constrained hydrological test site in North America.

2. Methodology

[4] In the following, we outline the methodological background of our approach. First, we introduce the forward modeling procedure that is used to simulate two synthetic cross-hole georadar data sets. These synthetic studies allow us to analyze the potential and limitations of the proposed approach. We then provide details on the processing and the subsequent tomographic inversion of the cross-hole georadar data. Finally, we discuss the cluster analysis approach for generating zoned aquifer models and discuss the models used in this study to estimate petrophysical properties of the resulting aquifer models.

2.1. Forward Modeling

[5] Our synthetic cross-hole georadar data are computed using a finite difference solution of Maxwell's equations in cylindrical coordinates that is fourth-order accurate in both time and space [*Bergmann et al.*, 1999; *Holliger and Bergmann*, 2002]. This efficient and accurate computational method predicts all direct, refracted and scattered electromagnetic waves and accounts for the inherent 3-D radiation and geometric spreading characteristics of dipole-type transmitters and receivers. The assumption of rotational symmetry with respect to the vertical axis implies a dominantly layered subsurface structure, which is generally justified for the near-surface alluvial environments considered here.

[6] The borehole georadar antennas are approximated by infinitesimal vertical electric dipoles. The emitted source pulse is a "Ricker" wavelet with a bandwidth of 2–3 octaves. The grid spacing was chosen to yield at least ten grid points per minimum wavelength. At this level of discretization, numerical inaccuracies due to grid dispersion are virtually negligible for our algorithm [*Bergmann et al.*, 1999]. Cylindrical symmetry conditions are applied along the left model edge and standard parabolic absorbing boundary conditions are employed along the top, bottom and right model edges. The efficiency of the absorbing boundaries is enhanced by a highly diffusive buffer zone of gradually decreasing resistivity with a thickness of several dominant wavelengths.

2.2. Data Processing and Inversion

[7] The synthetic and the observed cross-hole georadar data presented in this study are all processed and inverted following the guidelines provided by *Holliger et al.* [2001]. The travel times of the direct transmitted wave field are determined using a commercial semi-automated "picking" procedure. On the basis of these travel time picks, the maximum first-cycle amplitudes are then determined. Traces in which the direct transmitted wave clearly interfered with other wave types, such as waves refracted at the vadose zone boundary or at the Earth's surface, are not considered. The reason for this is that the corresponding amplitude behavior associated with different ray paths cannot be reliably reproduced with the ray-based method used for the inversion procedure. Prior to tomographic inversion, the picked amplitudes are corrected for the far-field directive properties of the transmitters and receivers, which we assume correspond to those of infinitesimal electrical dipoles in a homogeneous medium.

[8] The picked travel times are tomographically inverted for the velocity structure using a nonlinear inversion scheme based on a finite difference solution of the Eikonal equation [*Lanz et al.*, 1998]. Our approach fully accounts for the curvature of ray paths in heterogeneous media. The computed ray paths are then used to estimate geometric spreading factors and to tomographically reconstruct the attenuation structure [*Holliger et al.*, 2001].

[9] Ray-based amplitude tomography relies on a number of assumptions, many of which are probably rarely fully valid. The most important limitation of this method is clearly rooted in its inherent assumption of weak heterogeneity, which in turn implies negligible ray bending, no scattering, reflection or refraction effects, and largely undistorted full-space antenna radiation patterns. *Holliger et al.* [2001] and *Holliger and Maurer* [2002] have explored the implications of violations of these fundamental assumptions. They found that, although the absolute values of the inferred electrical conductivity may differ substantially from the actual values, the method is nevertheless useful and reliable for outlining the larger-scale conductivity structure as well as for constraining relative changes in conductivity. These results are consistent with those of a number of practical studies demonstrating the robustness of amplitude tomography and its potential to image subsurface features not detectable by travel time tomography alone [e.g., *Olsson et al.*, 1992; *Wright et al.*, 1996; *Valle et al.*, 1999; *Peterson*, 2001; *Zhou and Fullagar*, 2001].

2.3. Cluster Analysis

[10] Multivariate statistical methods, including cluster analysis techniques, are powerful tools for exploring and characterizing the relationships between various petrophysical parameters [e.g., *Gill et al.*, 1993; *Barrash and Morin*, 1997; *Bosch et al.*, 2002]. Because of their suitability for correlating and integrating information from a broad range of observations and for classifying data into homogeneous

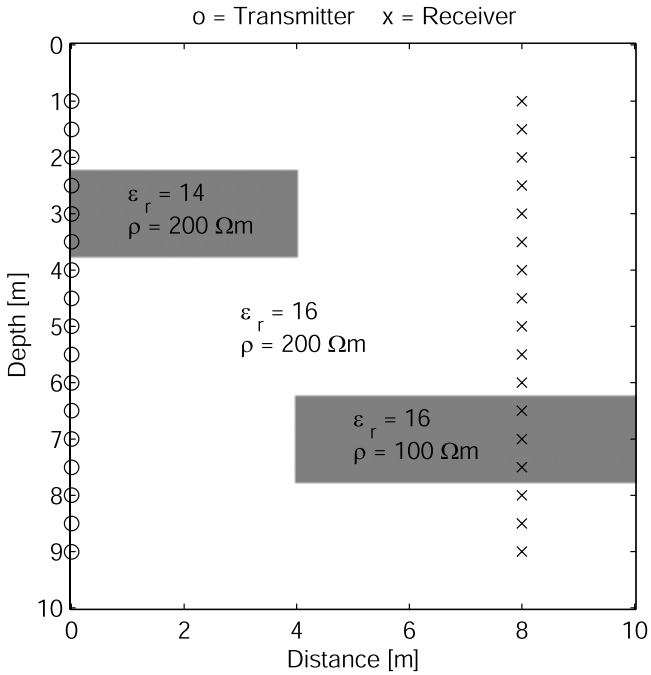

Figure 1. Model containing two anomalous bodies that differ from the matrix in terms of relative permittivity (ε_r) and electrical resistivity (ρ), respectively.

groups in the absence of a priori information on the groups, cluster techniques are widely used throughout the earth sciences [e.g., *Dumay and Fournier*, 1988; *Gill et al.*, 1993; *Fechner and Dietrich*, 1997; *Dietrich et al.*, 1998; *Hammah and Curran*, 1998; *Bosch et al.*, 2002; *Güler et al.*, 2002]. The fundamental principle of cluster analysis is to group data points in a multidimensional space on the basis of their distances (i.e., statistical measure of similarity) from each other. Unlike many other multivariate techniques, clustering methods do not assume a specific distribution (e.g., multivariate normal distribution) for the used variables. It should also be noted that correlated variables do not violate any fundamental assumptions in the cluster analysis.

[11] A distinction can be made between hierarchical and partitioning clustering approaches. Hierarchical techniques produce nested clusters (i.e., some clusters may be embedded in others), whereas partitioning techniques produce unitary partitioning into a predetermined number of homogeneous groups. Partitioning techniques are known to be less susceptible to outliers and to be computationally more efficient than hierarchical methods.

[12] A major objective of this study is to organize the often seeming erratic interrelationships between the tomographically determined velocity and attenuation structures in the shallow subsurface into a limited number of homogeneous groups as outlined above. This is most effectively achieved through a partitioning approach. In this study we use a partitioning technique known as *k*-means cluster analysis [*MacQueen*, 1967]. Because of its conceptual simplicity and algorithmic robustness, the *k*-means approach is one of the most popular and most widely used clustering techniques.

[13] On the basis of a qualitative assessment of cross plots of velocities and attenuations, suitably constrained by information on the subsurface structures, we first establish the number of clusters k that is required. Cluster formation then involves iterative regrouping of data points to minimize the variability in each cluster, that is to minimize the distances of the objects to the respective group center [*MacQueen*, 1967]. The final cluster distribution can be sensitive to the randomly selected initial partitioning and converge to a local minimum of the objective function. For this reason, the algorithm is run multiple times in order to ensure the stability of the final solution. The resulting velocity-attenuation clusters are characterized by the means and standard deviations of the two analyzed parameters. If the number of clusters cannot be specified reliably by a priori information or data analysis, statistical criteria, such as the widely used variance ratio criterion (VRC), can help to constrain the optimal number of clusters. The VRC method, originally introduced by *Calinski and Harabasz* [1974], uses the quotient between the intracluster average squared distance and inter-cluster average squared distance. The number of clusters that maximizes the value of the VRC is recommended as the optimal solution on the basis of this criterion. Further information on cluster analyses is given by *Kaufman and Rousseeuw* [1990] and *Everitt* [1993].

2.4. Parameter Estimation

[14] For each velocity-attenuation cluster in this study, we calculate the corresponding relative permittivity $\varepsilon_r = \varepsilon/\varepsilon_0$ and the electrical resistivity ρ using the high-frequency asymptotic equations for the velocity v and attenuation α of electromagnetic waves:

$$v \approx \sqrt{\frac{1}{\varepsilon\mu}}, \tag{1}$$

$$\alpha \approx \frac{1}{2\rho}\sqrt{\frac{\mu}{\varepsilon}}, \tag{2}$$

where ε and ε_0 are the permittivities of the probed material and free space, respectively, and μ is the magnetic permeability. Surficial soils and rocks are generally nonmagnetic such that we can assume $\mu = \mu_0$, where μ_0 is the magnetic permeability of a vacuum [*Davis and Annan*, 1989]. From the relative permittivity ε_r, we obtain first-order estimates of the porosity Φ for the clustered units using a two-component mixture model [*Wharton et al.*, 1980] for water-saturated media:

$$\Phi = \frac{\sqrt{\varepsilon_r} - \sqrt{\varepsilon_r^m}}{\sqrt{\varepsilon_r^w} - \sqrt{\varepsilon_r^m}}, \tag{3}$$

where ε_r^m and ε_r^w (= 80) are the relative permittivities of the dry matrix and water, respectively. On the basis of the results of a closely related case study of an alluvial aquifer [*Knoll and Clement*, 1999], we use $\varepsilon_r^m = 4.6$. Alternatively, the porosity Φ of saturated media can be estimated on the basis of a widely used empirical relation derived by *Topp et al.* [1980] relating the volumetric water content to ε_r. For fully saturated media, the volumetric water content is equal to Φ and Topp's equation can be written as:

$$\Phi = -5.3 \times 10^{-2} + 2.92 \times 10^{-2}\varepsilon_r - 5.5 \times 10^{-4}\varepsilon_r^2 + 4.3 \times 10^{-6}\varepsilon_r^3. \tag{4}$$

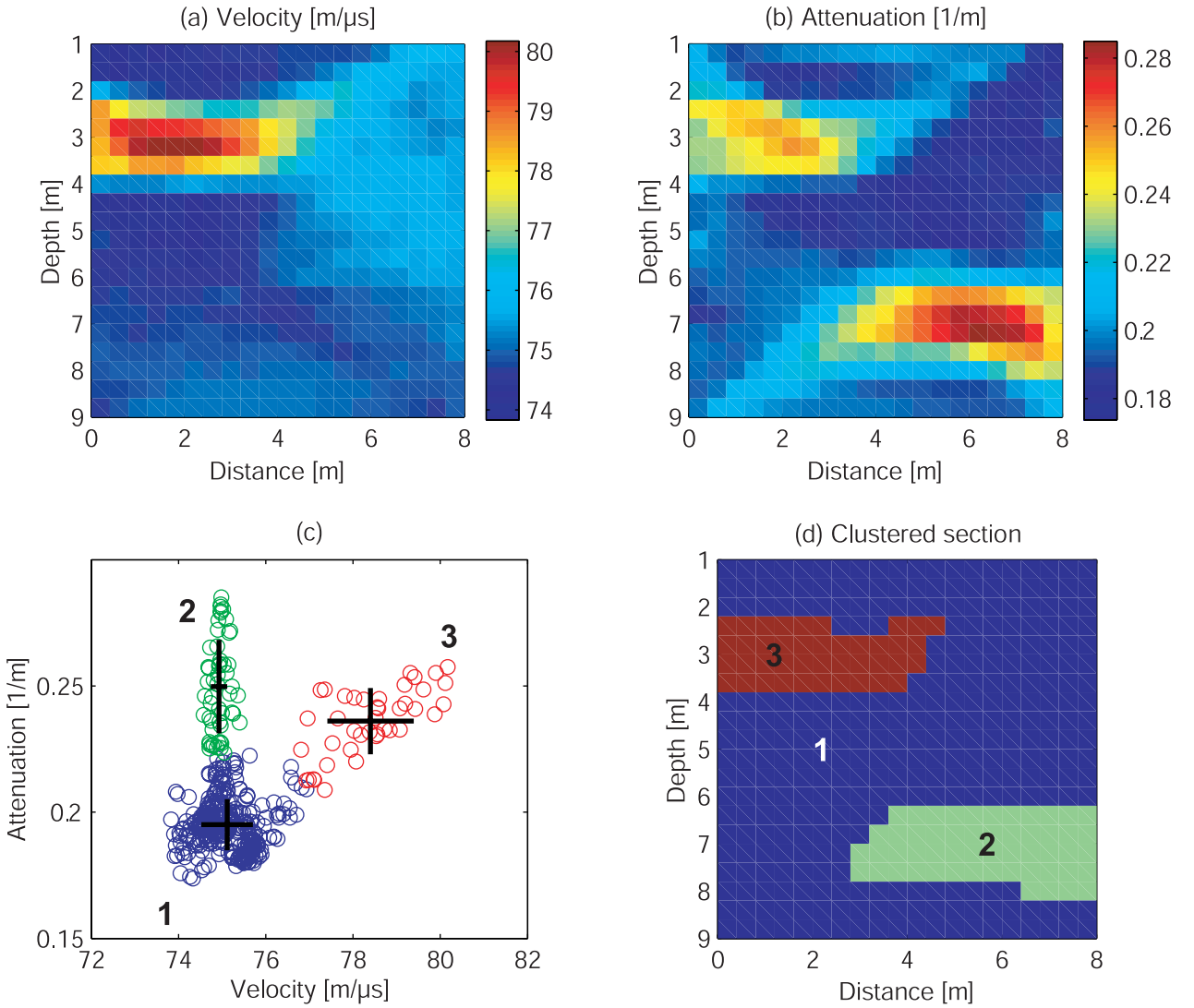

Figure 2. Results of ray-based tomographic inversion and subsequent cluster analysis for the model shown in Figure 1: (a) velocity distribution, (b) attenuation distribution, (c) cross plot of velocity versus attenuation, and (d) clustered section. In Figures 2c and 2d, numbers and color coding refer to specific clustered groups. In Figure 2c the crosses delineate cluster centers (mean values), with their dimensions equal to the respective standard deviations.

[15] Each cluster, then, is characterized by the means and standard deviations of the velocity, attenuation, relative permittivity, resistivity, and porosity that have been calculated using the respective parameter field. Mapping this information into the tomographically imaged subsurface yields a zoned subsurface image, which together with all available complementary information, forms the basis for a lithological and hydrological interpretation of the probed region.

3. Synthetic Examples

[16] In this section, we test the applicability, robustness and accuracy of our proposed method on two synthetic cross-hole georadar data sets of increasing complexity and realism. The purpose of these model studies is to explore the potential of this approach for identifying lithologically distinct and hydrologically relevant geological features and for estimating reliable averages of pertinent petrophysical parameters within these zones.

3.1. Block Model

[17] The first model is 9.0 × 8.0 m with a uniform grid spacing of 2.5 cm. It contains two block-shaped anomalies, one with an anomalous permittivity and one with an anomalous resistivity (Figure 1). The material properties in this example can be regarded as being typical of water-

Table 1. Cluster Statistics for the Block Model: Estimated Means ± Standard Deviation[a]

	Cluster 1	Cluster 2	Cluster 3
ε_r	15.95 ± 0.25 (16)	16.03 ± 0.08 (16)	14.65 ± 0.37 (14)
ρ	250.4 ± 12.9 (200)	195.5 ± 14.2 (100)	215.9 ± 10.6 (200)

[a]Respective input model values are shown in parentheses.

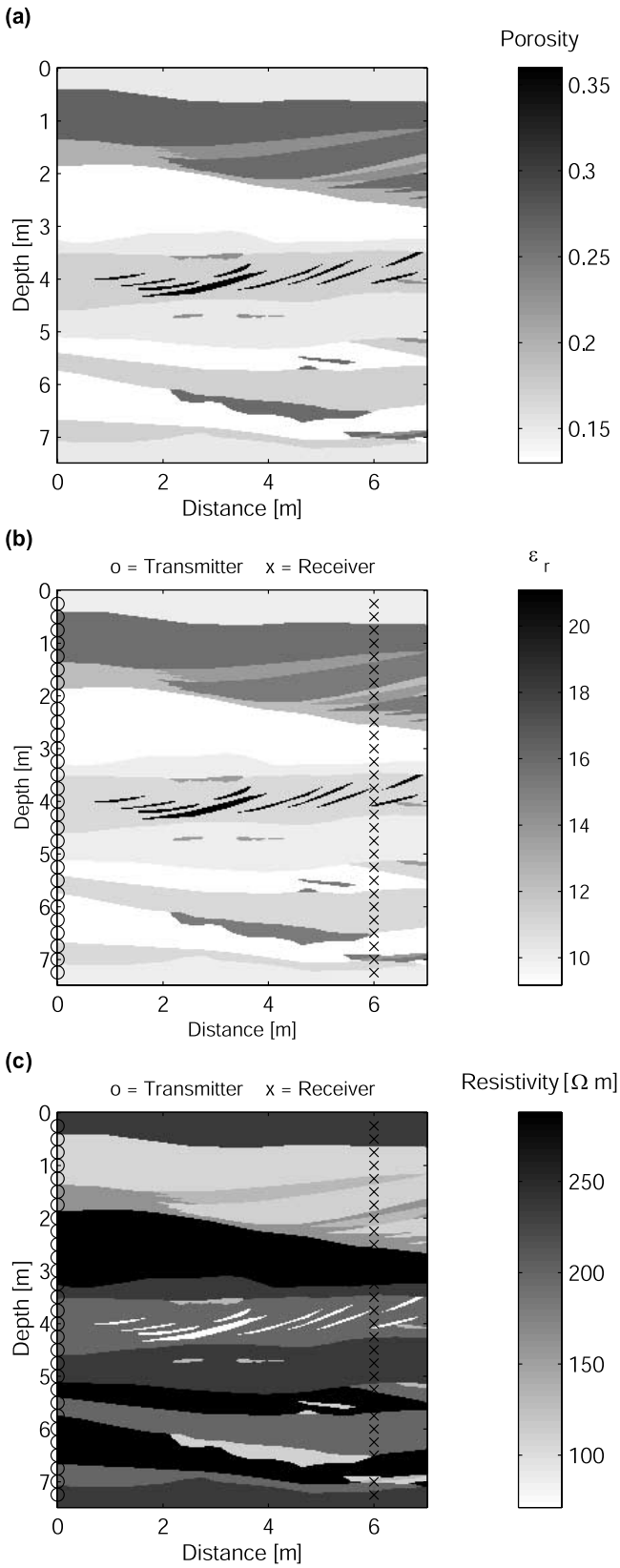

Figure 3. Outcrop-based model: (a) estimated porosity distribution, (b) relative permittivity distribution inferred from Figure 3a, and (c) electrical resistivity distribution inferred from Figure 3a.

saturated alluvial sediments with the two block-shaped bodies representing, for example, zones of lower porosity and higher clay content, respectively [*Davis and Annan*, 1989]. The source wavelet has a center frequency of 200 MHz, which corresponds to dominant wavelengths for the model of about 0.4 m. There are 17 transmitters and 17 receivers spaced at 0.5-m-intervals along the left and right sides of the model. This results in a total of 289 traces.

[18] The results of the tomographic inversion and subsequent grouping of velocity and attenuation values via cluster analysis are shown in Figures 2a–2d. The velocity tomogram (Figure 2a) clearly outlines the high-velocity zone corresponding to the anomalous body characterized by lower permittivities, but shows no indications of the resistivity anomaly. In the attenuation tomogram (Figure 2b), however, both anomalous bodies are seen as regions of elevated attenuation. The cross plot of velocities and attenuations shown in Figure 2c is the basis for the *k*-means cluster analysis. Even without a priori knowledge about the subsurface structure, a three-cluster-solution is an obvious choice for this example. In the resulting clustered section (Figure 2d), the matrix material (cluster 1) can be clearly discerned from the two anomalous bodies (clusters 2 and 3), the shapes and sizes of which are well resolved (Figure 2d). Finally, we used equations 1 and 2 to convert the mean values of each cluster (cluster centers in Figure 2c) into permittivity and resistivity and compared them to the original model values (Table 1). The discrepancies between the original and estimated permittivity and resistivity values are of the order of 0.0–4.6% and 8.0–95.5%, respectively. The high errors of some of the resistivity estimates most likely reflect the inherent limitations of ray-based attenuation estimates for energy traveling through heterogeneous media [*Holliger and Maurer*, 2002], as previously discussed in section 2.2. Thus the inferred resistivity structure should be regarded as largely qualitative in nature. Nevertheless, this example illustrates an important benefit of cross-hole georadar amplitude tomography, as the pure resistivity anomaly could not have been detected through travel time tomography alone.

3.2. Outcrop-Based Model

[19] The second model is based on outcrop evidence from a braided stream deposit observed in a gravel pit in the upper Rhine Valley of southwestern Germany. This outcrop is analyzed in detail by *Tronicke et al.* [2002a] who characterize various mapped lithological facies in terms of their porosities and hydraulic conductivities based on laboratory measurements. We use this outcrop section to develop a realistic model of a fully saturated heterogeneous alluvial aquifer.

[20] Following the work of *Kowalsky et al.* [2001], we use the measured porosities of the various sedimentary units (Figure 3a) to infer realistic model distributions of permittivity and resistivity (Figures 3b and 3c). Equation 3 is used to convert porosities into permittivities. To estimate resistivities, we employ the petrophysical model originally published by *Archie* [1942] for water-saturated sediments:

$$\rho = \frac{a}{\Phi^m}\rho_w. \tag{5}$$

The resistivity of the formation water ρ_w is assumed to be 20 Ωm, which is a realistic value for fresh groundwater. The

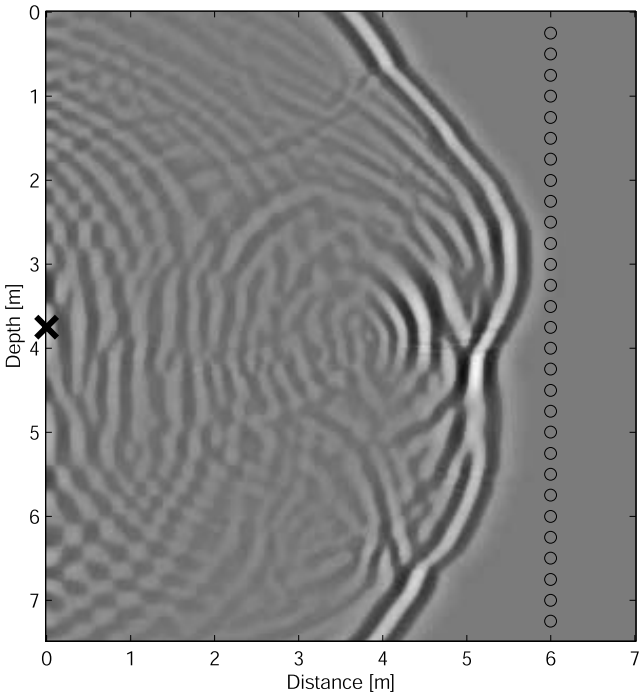

Figure 4. Snapshot of the vertical component of the electric field after propagating for 62 ns (about 14 dominant wavelengths) through the model shown in Figure 3. The plot illustrates the complexity of georadar wave propagation in a realistic, laterally heterogeneous alluvial aquifer. The source (denoted by a cross symbol) is located at a depth of 3.75 m. The receiver locations are denoted by circles.

values for a and m are chosen to be 0.88 and 1.37, respectively, which are considered to be typical values for the type of alluvial deposits considered here [*Schön*, 1998].

[21] The resulting model is 7.0 × 7.475 m with a uniform grid spacing of 2.5 cm. The source wavelet has a dominant frequency of 200 MHz, which corresponds to dominant wavelengths of 0.3 to 0.5 m for different regions of the model. Finite difference modeling is performed for 29 equally spaced transmitter and receiver stations located along the left and right sides of model (Figures 3b and 3c). This results in 841 synthetic georadar traces from which travel times and amplitudes are extracted. Figure 4 shows a snapshot of the propagating georadar wave field generated by a source at 3.75 m depth and illustrates the complexity of high-frequency electromagnetic wave propagation in such realistic heterogeneous settings. The snapshot is taken after a travel time of 62 ns. The vertical component of the electric field is plotted because it is this quantity that is recorded by a vertical dipole-type receiver. Following the direct wave we can see a number of scattered and reflected components of the wave field which interfere with the direct transmitted wave. It is important to note that the resulting "distortions" of the first-cycle amplitudes used for attenuation tomography cannot be accounted for by standard ray-based approaches [*Holliger and Maurer*, 2002].

[22] The results of the tomographic inversions and cluster analysis are shown in Figures 5a–5d. Although the velocities and attenuations both have an overall layered character (Figures 5a and 5b), as expected from the input model of Figure 3, correlation between most of the structures is not obvious. On the basis of the corresponding cross plot (Figure 5c), a four-cluster solution was chosen to represent the principal features common to the two tomographic images (Figure 5d). As illustrated by Figure 5e, this choice for optimal number of clusters, based on a qualitative a priori assessment of the tomographic images, is fully supported by the results of the VRC analysis. A comparison between Figures 3 and 5d indicates that the spatial distribution of the clustered units adequately mirrors the major lithological units of the input model. For example, the overall geometry of the slightly dipping high-porosity zone at 0.5 to 2 m depth is nicely outlined by cluster 1.

[23] To explore further the effectiveness of our approach, we estimated the permittivities, resistivities, and porosities using equations (1)–(4) and compared them with the parameters of the input model. Figures 6a, 6b, and 6c show these comparisons for the clustered units, whereas Figures 6d, 6e, and 6f show cross plots of the original model parameters and the parameters inferred using the geophysical attributes from the unclustered tomograms. For this purpose, the cell size of the model was resampled to 0.25 m using linear interpolation.

[24] As for the previous model (Figures 1 and 2), the overall parameter trends for the clustered units are correctly represented, but the means and standard deviations do not accurately represent the true model parameters (Figures 6a, 6b, and 6c). In particular, the contrasts in the electrical material parameters are underestimated by the tomographic inversions. This results from well-known limitations of the generally ill-conditioned and nonunique cross-hole tomographic problem [e.g., *Rector and Washbourne*, 1994; *Vasco et al.*, 1996], which has to be to stabilized by smoothing and damping constraints [*Menke*, 1984a; *Constable et al.*, 1987]. Increasing these regularization constraints reduces the model variance and thus acts as a spatial low-pass filter. Conversely, insufficient regularization fails to maintain sufficient a priori information to achieve a stable solution [e.g., *Clippard et al.*, 1995]. In Figure 6c the resistivity discrepancies for clusters 3 and 4 can be explained by the previously discussed inherent assumptions of ray-based methods for tomographic amplitude inversion. In the cross plots of the tomographically estimated parameters versus the original model parameters (Figures 6d, 6e, and 6f), it is again obvious that the tomographic parameter estimates do not account for the actual model variability. In these cross plots (particularly in Figure 6f), only weak linear relationships are apparent. This further serves to illustrate the

Figure 5. Results of ray-based tomographic inversion and subsequent cluster analysis for the outcrop analog model shown in Figure 3: (a) velocity distribution, (b) attenuation distribution, (c) cross plot of velocity versus attenuation, (d) clustered section, and (e) VRC value as function of the number of clusters. In Figures 5a and 5b, poorly resolved regions (i.e., those with poor ray coverage) are blanked out. In Figures 5c and 5d, numbers and colors refer to specific clusters. In Figure 5c the crosses delineate cluster centers (mean values), with their dimensions equal to the respective standard deviations. In Figure 5d, black lines outline the major zones of the input model (Figure 3).

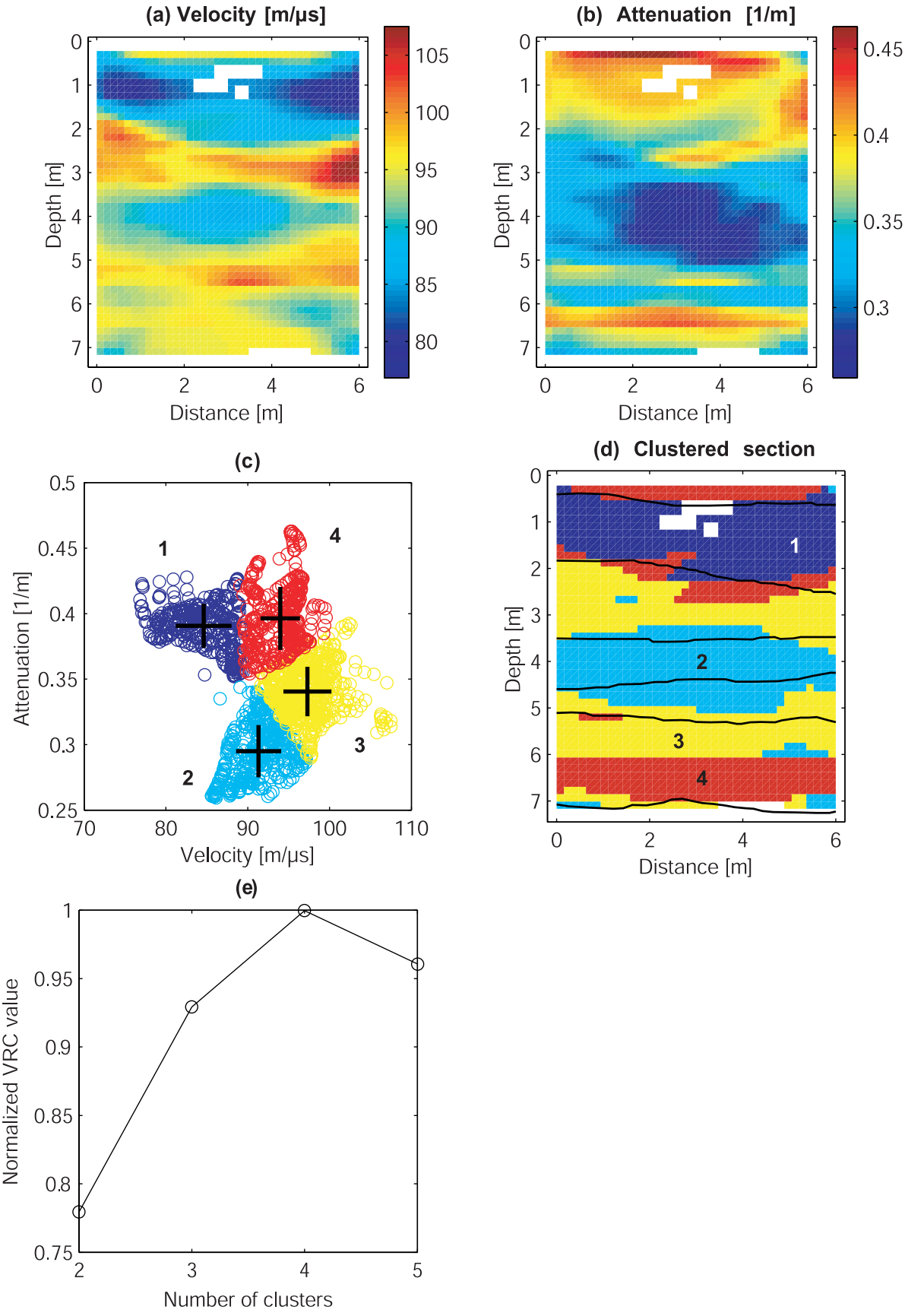
(a) Velocity [m/µs]
Depth [m]
Distance [m]
105
100
95
90
85
80
(b) Attenuation [1/m]
Depth [m]
Distance [m]
0.45
0.4
0.35
0.3
(c)
Attenuation [1/m]
Velocity [m/µs]
1
2
3
4
(d) Clustered section
Depth [m]
Distance [m]
1
2
3
4
(e)
Normalized VRC value
Number of clusters

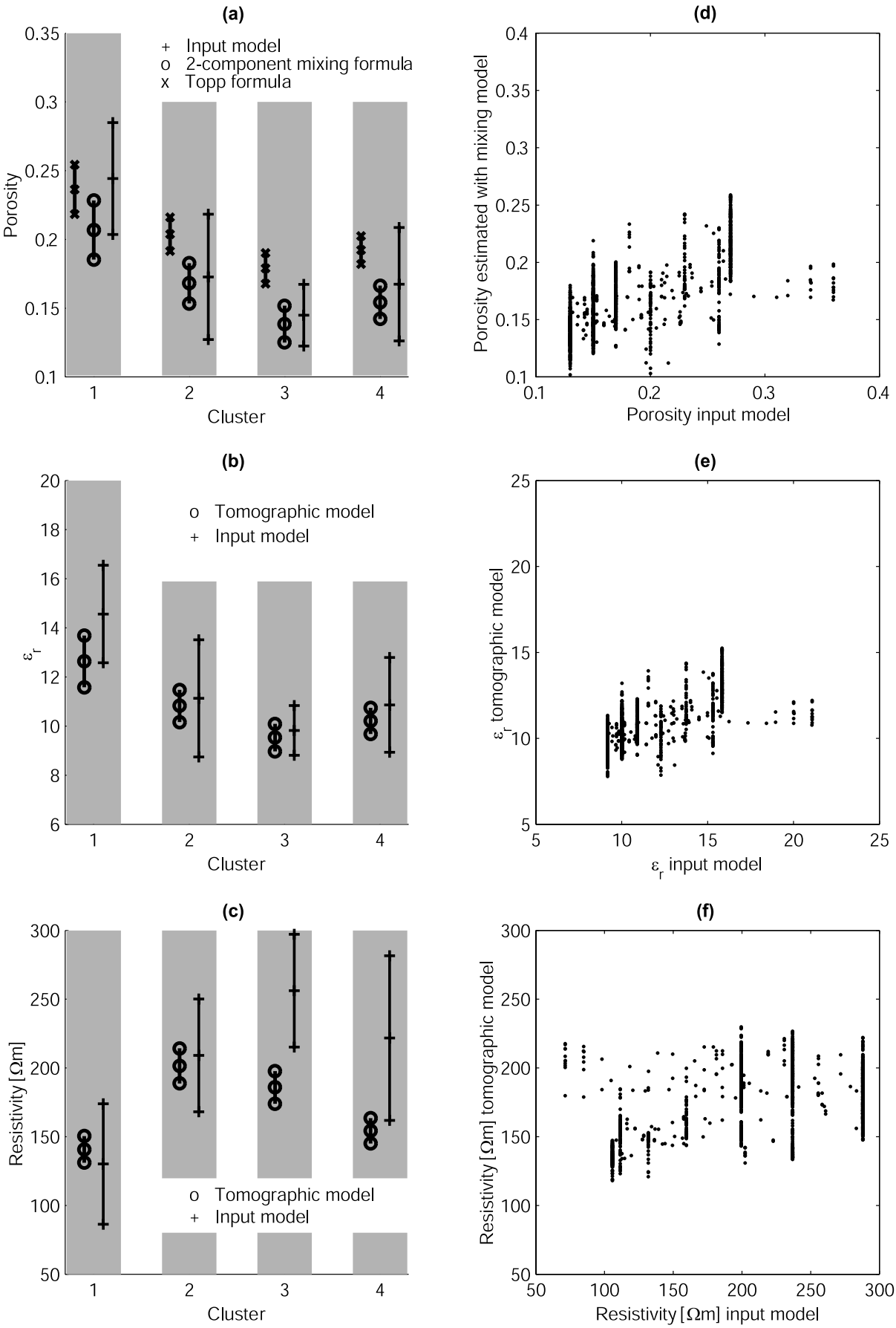
(a)
+ Input model
o 2-component mixing formula
x Topp formula
Porosity
Cluster
(b)
o Tomographic model
+ Input model
ε_r
Cluster
(c)
o Tomographic model
+ Input model
Resistivity [Ωm]
Cluster
(d)
Porosity estimated with mixing model
Porosity input model
(e)
ε_r tomographic model
ε_r input model
(f)
Resistivity [Ωm] tomographic model
Resistivity [Ωm] input model

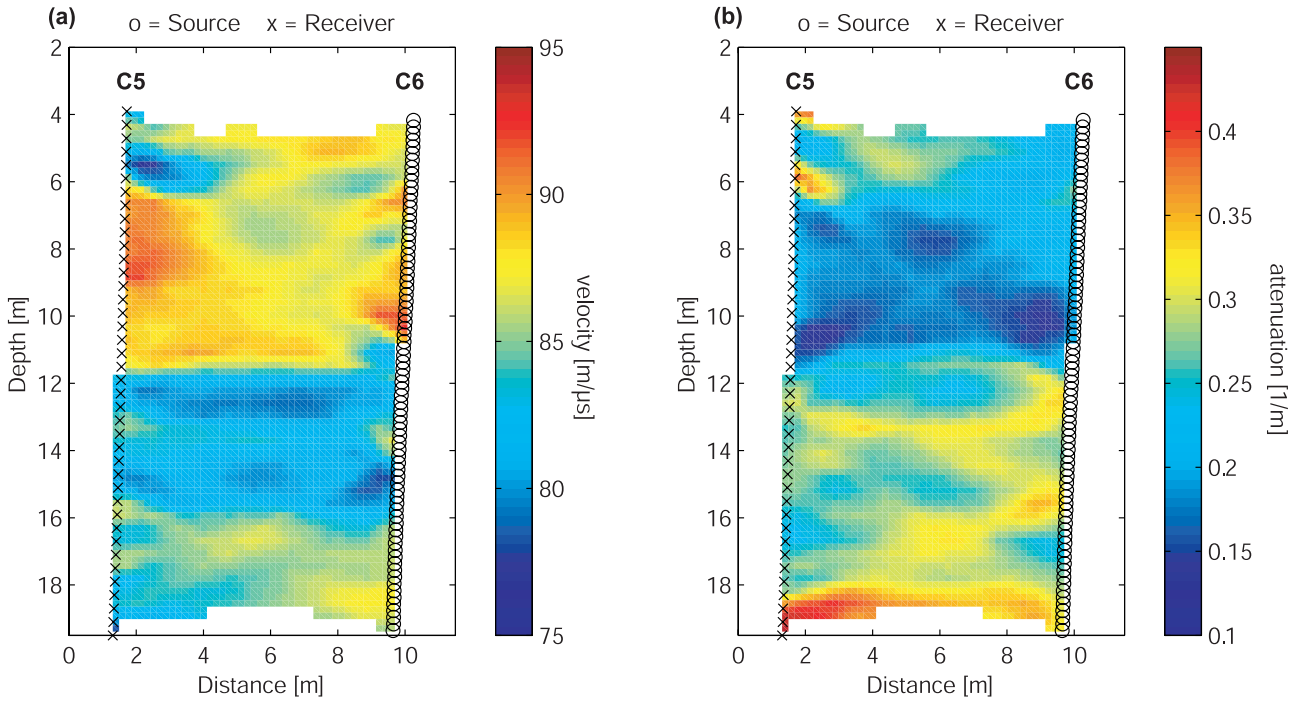

Figure 7. Results of ray-based tomographic inversion of a cross-hole georadar data set recorded at the Boise Hydrogeophysical Research Site (BHRS): (a) velocity distribution and (b) attenuation distribution. Poorly resolved regions (i.e., those with poor ray coverage) are blanked out. The groundwater table is at a depth of 2.96 m.

potential benefits of "reducing" the rather complex tomographic images to a limited number of clusters. Although the absolute values of the inverted parameters can only be regarded as approximations, the multivariate grouping process enables us to identify major trends in the petrophysical properties.

4. Field Data Example

[25] We now apply our new procedure to a cross-hole georadar data set collected at the Boise Hydrogeophysical Research Site (BHRS) near Boise, Idaho. This research site was established to develop and calibrate hydrogeological and geophysical methods for determining the 3-D distribution of hydraulic parameters in unconsolidated heterogeneous alluvial deposits [*Barrash and Knoll*, 1998; *Clement et al.*, 1999]. The subsurface at this site is characterized by an approximately 20-m-thick alluvial layer consisting predominantly of gravel and sand with minimal fractions of silt and clay. Underneath is a >3 m thick layer of red clay. At the time of the measurements (October 1998), the water table was at depth of 2.96 m.

[26] The cross-hole georadar data set was acquired using two near-vertical boreholes C5 and C6, which have a diameter of 10.2 cm and are approximately 8.5 m apart (Figure 7). Although the borehole georadar antennas were reported to have a nominal frequency of 250 MHz, we found that the observed data had a dominant frequency below 100 MHz. The primary reason for this is that the nominal antenna frequency refers to its performance in free-space, whereas the low velocities of the water in the borehole and the surrounding water-saturated sediments make the antenna "electrically longer" and thus reduce its resonance frequency. Several surface walk-away measurements were used to determine a correction for time-zero and observe possible time drifts during the survey. Care was taken that the antennas were moved quite slowly through the borehole with respect to the recording time of an individual data trace in order to avoid data smearing. The fact that the diameter of the antennas (~5 cm) is not much smaller than that of the boreholes causes the antennas to be naturally centralized, which should ensure stable coupling conditions for the antennas to the borehole and surrounding medium. The experimental setup consisted of 77 transmitter stations and 40 receiver stations spaced at 0.2 and 0.4 m intervals, respectively. From the resultant 3080 traces, 2064 could be employed for the combined tomographic imaging process. Preprocessing of the data included removal of the DC component and application of a 0–250 MHz zero-phase low-pass filter.

Figure 6. Comparison of the actual input parameters of the outcrop-based model (Figure 3) with the corresponding estimates obtained from the tomographic inversion of the synthetic crosshole georadar survey (Figures 4 and 5). The diagrams in the left column show comparisons of mean values (centers of vertical bars) and standard deviations (lengths of vertical bars) of (a) porosity, (b) relative permittivity, and (c) electric resistivity for the clustered section (Figure 5d). The right column shows cross plots of (d) porosity, (e) relative permittivity, and (f) electric resistivity based on the original input model (Figure 3) and the unclustered tomographic sections (Figures 5a and 5b).

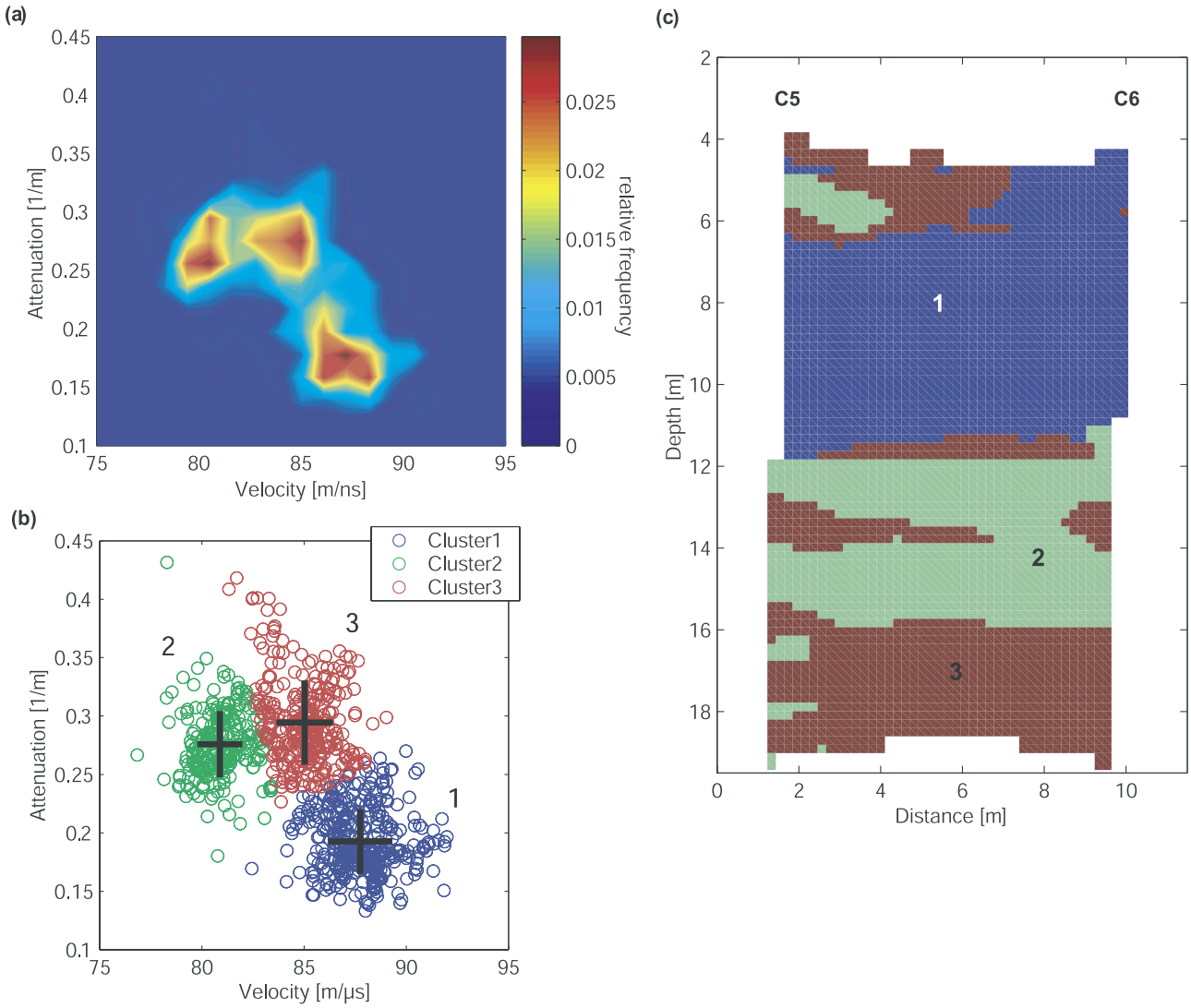

Figure 8. (a) Contoured histographic plot (19 × 19 bins considered) illustrating trends in the velocity-attenuation relationship. (b) Cross plot of velocity versus attenuation. Crosses delineate cluster centers (mean values), with their dimensions equal to the respective standard deviations. (c) Results of cluster analysis of the BHRS cross-hole georadar tomograms visualized as spatial distributions of cluster membership between boreholes C5 and C6. In Figures 8c and 8d, numbers and colors refer to specific clusters.

[27] The resulting tomographic images are shown in Figure 7. Both the velocity and attenuation tomograms are distinguished by predominantly subhorizontal structures, which is consistent with stratigraphic layering in the gravel and sand deposits at the BHRS [*Barrash and Clemo*, 2002]. Except for the strong bimodal distribution of values centered about a horizontal line at 11.8 m depth, there does not seem to be a clear and/or systematic relationship between the velocity and attenuation tomograms.

[28] Figure 8a shows a contoured histographic plot of the estimated velocities and attenuations. Given that this plot is characterized by three distinct and clearly separated maxima, we choose a three-cluster solution for further analysis (Figure 8b). Cluster 1 is characterized by higher velocities and lower attenuations than clusters 2 and 3. Clusters 2 and 3 are distinguished from each other only by their velocities. The resulting spatial distribution of clusters in the tomographic plane is shown in Figure 8c. Although the characterization of the subsurface has been reduced to only three petrophysical parameter groupings, the clustered section retains the major structural features of the original tomograms (Figure 7).

[29] As for the synthetic examples, we proceed by deriving estimates of the relative permittivities, resistivities and porosities of the clustered units using equations (1), (2) and (4), respectively. We use Topp's equation (4) to estimate the porosity distribution. The reason for this choice is that the relative dielectric permittivity of the dry matrix, which is a key parameter of the mixing model (3), is not explicitly known. We then compare the clustered porosities and resistivities along the boreholes to corresponding logging data and to the corresponding tomographically inferred material properties representing the tomographic values (Figure 9 and Table 2) close to the boreholes. In so doing,

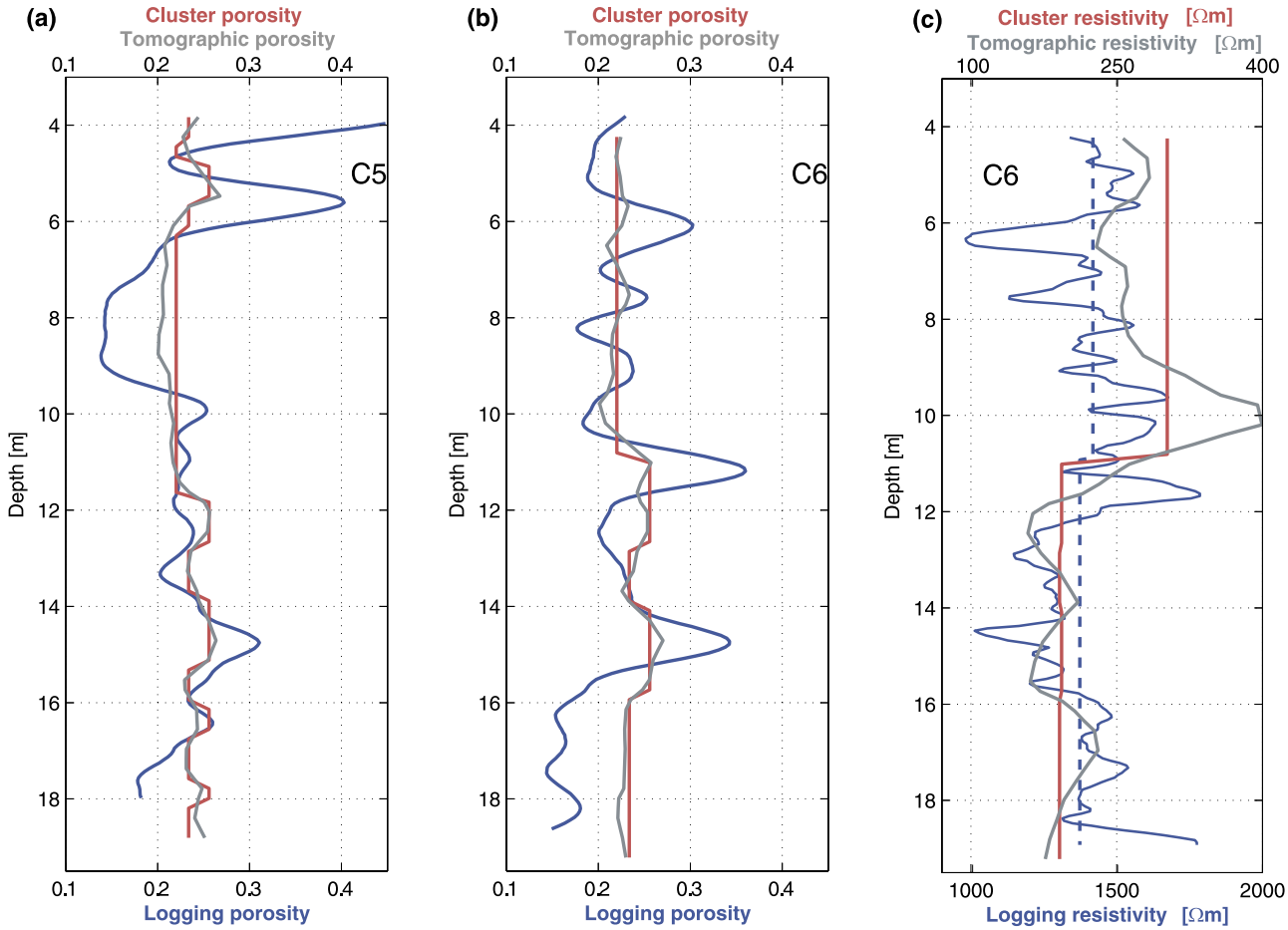

Figure 9. Comparison of logging data (blue lines, lower horizontal axis) with corresponding clustered tomographic (red lines, upper horizontal axis) and unclustered tomographic (gray lines, upper horizontal axis) parameter estimates along the boreholes: (a) neutron porosity log versus clustered and unclustered tomographic porosities for borehole C5, (b) neutron porosity log versus clustered and unclustered tomographic porosities for borehole C6, and (c) capacitive resistivity log versus clustered and unclustered tomographic resistivity for borehole C6. In Figure 9c, note the different scaling of the lower and upper horizontal axes for the log data and the clustered parameter estimates, respectively. In Figure 9c the dashed blue line represents mean logging resistivity values for the two major resistivity zones visible in the clustered model.

it is necessary to emphasize that the clustered parameter estimates are based on spatially averaged information that is representative of the entire probed region, whereas the logging data reflect the in situ variations of these parameters in the immediate vicinity of the boreholes. Moreover, we have to consider limited resolution in the plotted tomographically inferred material properties in Figure 9 because the resolution of cross-hole tomographic images is inherently limited in the vertical direction and poorly constrained near the boreholes [*Menke*, 1984b].

[30] Figures 9a and 9b compare the porosities estimated for the clustered units with the tomographically inferred porosity estimates and the neutron log porosities along boreholes C5 and C6 [*Barrash and Clemo*, 2002], respectively. The continuous porosity profiles estimated from the velocity tomogram as well as the corresponding clustered version faithfully reproduce the overall pattern and the larger-scale trend delineated by the neutron porosity logs. In particular, most high-porosity zones present in the porosity logs are also present as high-porosity zones in the clustered porosity section (see also Table 2). The clustered tomographic image thus confirms and extends the hydrological zonation proposed by *Barrash and Clemo* [2002], which was largely based on 1-D evidence from log data.

[31] In addition to the neutron porosity logs, capacitive resistivity logging data [*Mwenifumbo and Bristow*, 1999] are available for borehole C6. To date, accurate calibration of this logging tool is not available for unconsolidated coarse alluvial sediments, such as those at the BHRS, but there is high confidence with regard to the relative changes in the logging data from C6 (C. J. Mwenifumbo, personal communication). In Figure 9c we compare these data to the resistivity estimates along borehole C6 extracted from the attenuation tomogram and from our clustered model (Figure 8c). As with the porosity estimates, the tomographic resistivity profile reliably captures the major trends in the logging data. The clustered resistivities are characterized by a relatively high-resistivity unit down to a depth of about 11 m, and a lower-resistivity unit below. Although the

Table 2. Statistics for the Clustered Model for the BHRS Field Data Set, for the Corresponding Unclustered Tomographic Data Close to the Boreholes Within the Clustered Units and for the Logging Data Within the Clustered Units[a]

	Cluster 1	Cluster 2	Cluster 3
	Clustered Tomographic Data		
Φ	0.220 ± 0.008	0.256 ± 0.007	0.234 ± 0.007
ρ	301.4 ± 43.3	192.09 ± 19.9	189.99 ± 22.6
	Unclustered Tomographic Data Along Boreholes		
Φ	0.217 ± 0.010	0.253 ± 0.008	0.233 ± 0.007
ρ	285.8 ± 48.9	185.5 ± 32.1	199.2 ± 17.8
	Logging Data		
Φ	0.211 ± 0.042	0.257 ± 0.049	0.226 ± 0.073
ρ	1419.26 ± 151.1	1349.8 ± 184.8	1397.9 ± 129.6

[a]See Figure 9. The values denote estimated means ± standard deviations. Please note that the resistivity values from the logging data are subject to an unknown bias and hence can only be assessed in terms of the relative variations.

resistivity log exhibits much more small-scale structural complexity, its large-scale pattern (plotted means for the major units in Figure 9c) is consistent with the results of the cluster analysis (see also Table 2). For all these comparisons, it should be again noted that the resolution of cross-hole tomographic images is inherently limited along the boreholes, that porosity logs may be affected by distortions in the vicinity of the boreholes due to the drilling process, and that the spatial resolution of the two methods (i.e., logging and cross-hole tomography) differs roughly by one order-of-magnitude.

[32] As a final check on the validity of our approach, we compare an observed radar section with corresponding synthetic radar sections based on the original tomograms and based on the corresponding clustered section (Figures 10a–10c). On the basis of averaged spectral analyses of the observed cross-hole georadar data, the dominant frequency of the source wavelet is set to 70 MHz, which yields a dominant wavelength of about 1 m. The grid spacing is 8 cm. A 9-m-wide diffusive buffer zone is added to the top, bottom and right model edges in order to avoid artificial reflections from the boundaries of the computational domain. The resulting synthetic georadar sections reproduce the detailed character of the direct transmitted wave in the observed data. Moreover, the synthetic section determined from the model defined by the original tomograms also reproduces the overall character of reflected and scattered secondary arrivals present in the observed data (Figures 10a and 10b). We conclude that the tomographic images are realistic representations of the subsurface structure and that the dominant features of this structure are adequately captured by the corresponding clustered sections.

5. Conclusions

[33] We have explored the potential of applying cluster analysis to cross-hole georadar velocity and attenuation tomograms as a means to define hydrological zones within unconsolidated alluvial aquifers. Synthetic studies illustrate that, even for complex models, the major lithological and petrophysical trends can be resolved by ray-based tomographic inversion of cross-hole georadar travel times and amplitudes. There can, however, be significant discrepancies between absolute values of the inverted petrophysical parameters and the model parameters. These discrepancies are particularly pronounced for petrophysical parameters based on the attenuation estimates. This shortcoming largely reflects the inherent limitations of ray-based tomographic methods and could be alleviated through the development and application of full-waveform inversion algorithms.

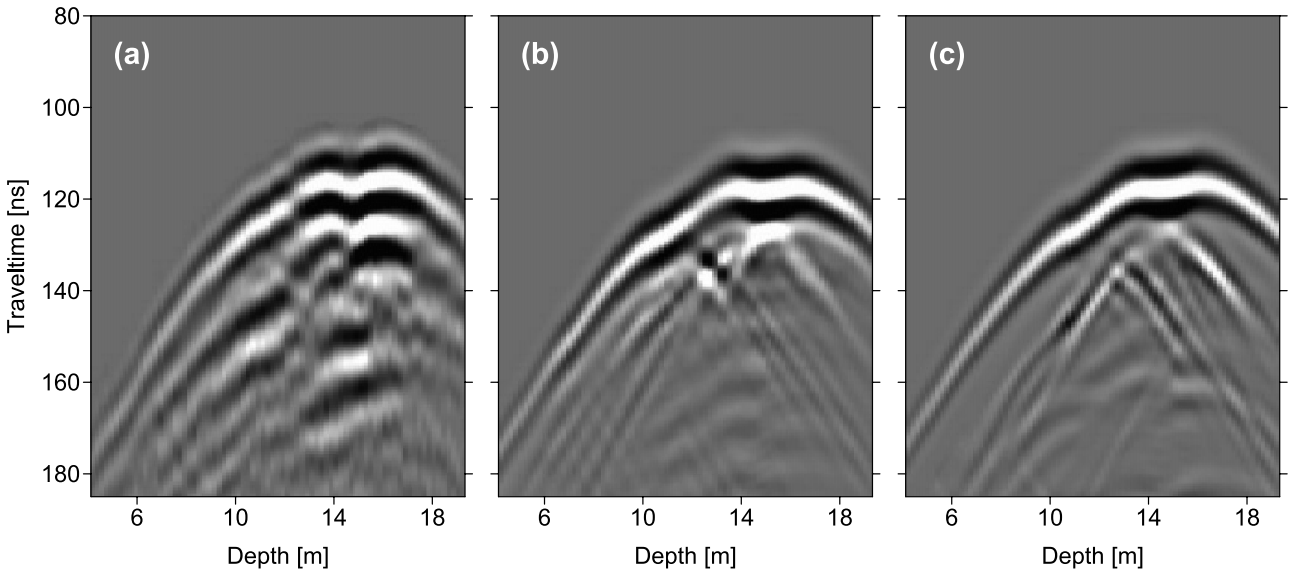

Figure 10. Comparison of observed and simulated cross-hole georadar data gathers at the BHRS. (a) Observed data gather after minor processing, (b) synthetic data gather based on the inverted velocity and attenuation tomograms (Figure 7), and (c) synthetic data gather based on the clustered model (Figure 9). Each gather is scaled with a separate time-dependent scaling function to preserve relative amplitude changes. For all gathers the fixed antenna is located at a depth of 14.66 m.

[34] Cluster analysis proved to be a powerful postprocessing tool for correlating and integrating the generally complex relationships between the tomographically determined velocity and attenuation structures. The technique is suitable for detecting and quantifying common trends in velocity and attenuation tomograms by grouping the tomographic information into a limited number of characteristic parameter combinations. On the basis of our synthetic studies, we found that the clustered sections adequately outline the pertinent features of the input models and allow for more meaningful petrophysical parameter estimates compared to estimates based on the un-clustered tomographic parameter fields. We conclude that cluster analysis helps to determine the pertinent trends and groupings in a multivariate geophysical data set based on objective criteria.

[35] Our approach was successfully applied to a cross-hole georadar data set collected in a well-studied alluvial aquifer. Porosities and resistivities inferred from the clustered tomograms were compared to corresponding borehole log data. We found that the clustered porosity section predicted the overall zonation delineated by the neutron porosity log. In particular, it located most high-porosity zones present in the log data. Furthermore, we found reasonable agreement between the clustered resistivities along one borehole and the large-scale trend of capacitive resistivity logging.

[36] On the basis of the results of this study, we suggest that a combination of clustered georadar tomographic sections and corresponding logging data may be used to develop site-specific hydrological models. This could, for example, be achieved by assigning pertinent parameters obtained from porosity logs (e.g., mean values, standard deviations and correlation lengths) to the corresponding units in the clustered tomographic section. This approach could be extended to establish relationships between the clustered tomographic sections and estimates of hydraulic conductivity obtained, for example, from flowmeter logs or grain size analyses.

[37] **Acknowledgments.** This research was supported by grant 2-77087-01 from the Swiss National Science Foundation (JT and KH) and by U.S. Army Research Office grants DAAH04-96-1-0318 and DAAG55-98-1-0277 (WB and MDK). The first author also acknowledges financial support by the German Science Foundation (DFG) for sponsoring a research fellowship at CGISS, Boise State University, Idaho, USA, where parts of the presented work were carried out. The outcrop analog data were gathered and analyzed as part of DFG project SFB275/TPC3 at the Institute of Geology, University of Tübingen, Germany. We thank Bill Clement for helping with the field work, Peter Dietrich for providing his *k*-means cluster analysis code, Jonathan Mwenifumbo for supplying the capacitive resistivity data, and Alan G. Green for an in-house review. This is ETH-Geophysics contribution 1309.

References

Anderson, M. P. (1989), Hydrogeologic facies models to delineate large-scale spatial trends in glacial and glaciofluvial sediments, *Geol. Soc. Am. Bull.*, *101*(4), 501–511.

Archie, G. E. (1942), The electrical resistivity log as an aid in determining some reservoir characteristics, *Trans. Am. Inst. Min. Metall. Pet. Eng.*, *146*, 54–62.

Asprion, U., and T. Aigner (1999), Towards realistic aquifer models: Three-dimensional georadar surveys of Quaternary gravel deltas (Singen basin, SW-Germany), *Sediment. Geol.*, *129*(3–4), 281–297.

Barrash, W., and T. Clemo (2002), Hierarchical geostatistics and multifacies systems: Boise Hydrogeophysical Research Site, Boise, Idaho, *Water Resour. Res.*, *38*(10), 1196, doi:10.1029/2002WR001436.

Barrash, W., and M. D. Knoll (1998), Design of research wellfield for calibrating geophysical methods against hydrologic parameters, paper presented at 1998 Conference on Hazardous Waste Research, Great Plains/Rocky Mtn. Hazard. Substance Res. Cent., Snowbird, Utah.

Barrash, W., and R. H. Morin (1997), Recognition of units in coarse, unconsolidated braided-stream deposits from geophysical log data with principal components analysis, *Geology*, *25*(8), 687–690.

Beres, M., and F. P. Haeni (1991), Application of ground-penetrating-radar methods in hydrogeologic studies, *Ground Water*, *29*(3), 375–387.

Bergmann, T., J. O. Blanch, J. O. A. Robertsson, and K. Holliger (1999), A simplified Lax-Wendroff correction for staggered-grid FDTD modeling of electromagnetic wave propagation in frequency-dependent media, *Geophysics*, *64*(5), 1369–1377.

Binley, A., P. Winship, R. Middleton, M. Pokar, and J. West (2001), High-resolution characterization of vadose zone dynamics using cross-borehole radar, *Water Resour. Res.*, *37*(11), 2639–2652.

Bosch, M., M. Zamora, and W. Utama (2002), Lithology discrimination from physical rock properties, *Geophysics*, *67*(2), 573–581.

Calinski, T., and J. Harabasz (1974), A dendrite method for cluster analysis, *Commun. Stat.*, *3*, 1–27.

Chen, J., S. Hubbard, and Y. Rubin (2001), Estimating hydraulic conductivity at the South Oyster Site from geophysical tomographic data using Bayesian techniques based on the normal regression model, *Water Resour. Res.*, *37*(6), 1603–1613.

Clement, W. P., M. D. Knoll, L. M. Liberty, P. R. Donaldson, P. Michaels, W. Barrash, J. R. Pelton (1999), Geophysical surveys across the Boise Hydrogeophysical Research Site to determine geophysical parameters of a shallow, alluvial aquifer, paper presented at SAGEEP99, The Symposium on the Application of Geophysics to Engineering and Environmental Problems, Environ. and Eng. Geophys. Soc., Oakland, Calif.

Clippard, J. D., D. H. Christensen, and R. D. Rechtien (1995), Composite distribution inversion applied to crosshole tomography, *Geophysics*, *60*(5), 1283–1294.

Constable, S. C., R. L. Parker, and C. G. Constable (1987), Occam's inversion: A practical algorithm for generating smooth models from electromagnetic sounding data, *Geophysics*, *52*(3), 289–300.

Corbeanu, R. M., K. Soegaard, R. B. Szerbiak, J. B. Thurmond, G. A. McMechan, D. Wang, S. H. Snelgrove, C. B. Forster, and A. Menitove (2001), Detailed internal architecture of a fluvial channel sandstone determined from outcrop, cores, and 3-D ground-penetrating radar: Example from the middle Cretaceous Ferron Sandstone, east-central Utah, *AAPG Bull.*, *85*(9), 1583–1608.

Davis, J. L., and A. P. Annan (1989), Ground-penetrating radar for high-resolution mapping of soil and rock stratigraphy, *Geophys. Prospect.*, *37*(5), 531–551.

Dietrich, P., T. Fechner, J. Whittaker, and G. Teutsch (1998), An integrated hydrogeophysical approach to subsurface characterization, in *Groundwater Quality: Remediation and Protection*, edited by K. Herbert and M. Kovar, *IAHS Publ.*, *250*, 513–519.

Dumay, J., and F. Fournier (1988), Multivariate statistical analyses applied to seismic facies recognition, *Geophysics*, *53*(9), 1151–1159.

Everitt, B. S. (1993), *Cluster Analysis*, 170 pp., Edward Arnold, London.

Fechner, T., and P. Dietrich (1997), Lithological inversion of tomographic data, paper prestented at 3rd Annual Meeting, Eur. Sect., Environ. and Eng. Geophys. Soc., Aarhus, Denmark.

Gill, D., A. Shomrony, and H. Fligelman (1993), Numerical zonation of log suites and logfacies recognition by multivariate clustering, *AAPG Bull.*, *77*(10), 1781–1791.

Goldstein, S. E., T. C. Johnson, M. D. Knoll, W. Barrash, and W. P. Clement (2003), Borehole radar attenuation tomography during the tracer/time-lapse test at the Boise Hydrogeophysical Research Site, paper presented at SAGEEP03, The Symposium on the Application of Geophysics to Engineering and Environmental Problems, Environ. and Eng. Geophys. Soc., San Antonio, Tex.

Greaves, R. J., D. P. Lesmes, J. M. Lee, and M. N. Toksöz (1996), Velocity variations and water content estimated from multi-offset, ground-penetrating radar, *Geophysics*, *61*(3), 683–695.

Güler, C., G. D. Thyne, J. E. McCray, and A. K. Turner (2002), Evaluation of graphical and multivariate statistical methods for classification of water chemistry data, *Hydrogeol. J.*, *10*(4), 455–474.

Hammah, R. E., and J. H. Curran (1998), Fuzzy cluster algorithm for the automatic identification of joint sets, *Int. J. Rock Mech. Min. Sci.*, *35*(7), 889–905.

Holliger, K., and T. Bergmann (2002), Finite-difference modeling of borehole georadar data, *Geophysics*, *67*(4), 1249–1257.

Holliger, K., and H. R. Maurer (2002), Effects of stochastic heterogeneity on the tomographic inversion of crosshole georadar data, paper presented at 72nd Annual Meeting, Soc. of Explor. Geophys., Salt Lake City, Utah.

Holliger, K., M. Musil, and H. R. Maurer (2001), Ray-based amplitude tomography for crosshole georadar data: a numerical assessment, *J. Appl. Geophys.*, *47*(3–4), 285–298.

Hubbard, S., J. E. Peterson, J. Roberts, and F. Wobber (1997), Estimation of permeable pathways and water content using tomographic radar data, *Leading Edge*, *16*(11), 1623–1628.

Hubbard, S., J. Chen, J. E. Peterson, E. L. Majer, K. H. Williams, D. J. Swift, B. Mailloux, and Y. Rubin (2001), Hydrogeological characterization of the South Oyster Bacterial Transport Site using geophysical data, *Water Resour. Res.*, *37*(10), 2431–2456.

Hyndman, D. W., and S. M. Gorelick (1996), Estimating lithologic and transport properties in three dimensions using seismic and tracer data: The Kesterson aquifer, *Water Resour. Res.*, *32*(9), 2659–2670.

Hyndman, D. W., J. M. Harris, and S. M. Gorelick (2000), Inferring the relation between seismic slowness and hydraulic conductivity in heterogeneous aquifers, *Water Resour. Res.*, *36*(8), 2121–2132.

Jussel, P., F. Stauffer, and T. Dracos (1994), Transport modeling in heterogeneous aquifers: 1. Statistical description and numerical generation of gravel deposits, *Water Resour. Res.*, *30*(6), 1803–1817.

Kaufman, L., and P. J. Rousseeuw (1990), *Finding Groups in Data: An Introduction to Cluster Analysis*, 342 pp., John Wiley, Hoboken, N. J.

Klingbeil, R., S. Kleineidam, U. Asprion, T. Aigner, and G. Teutsch (1999), Relating lithofacies to hydrofacies: Outcrop-based hydrogeological characterisation of Quaternary gravel deposits, *Sediment. Geol.*, *129*(3–4), 299–310.

Knoll, M. D., and W. P. Clement (1999), Vertical radar profiling to determine dielectric constant, water content and porosity values at well locations, paper presented at SAGEEP99, The Symposium on the Application of Geophysics to Engineering and Environmental Problems, Environ. and Eng. Geophys. Soc, Oakland, Calif.

Kowalsky, M. B., P. Dietrich, G. Teutsch, and Y. Rubin (2001), Forward modeling of ground-penetrating radar data using digitized outcrop images and multiple scenarios of water saturation, *Water Resour. Res.*, *37*(6), 1615–1625.

Lanz, E., H. R. Maurer, and A. G. Green (1998), Refraction tomography over a buried waste disposal site, *Geophysics*, *63*(4), 1414–1433.

MacQueen, J. (1967), Some methods for classification and analysis of multivariate observations, in *Proceedings of 5th Berkeley Symposium on Mathematics, Statistics and Probability*, pp. 281–297, Univ. of Calif., Berkeley.

Menke, W. (1984a), *Geophysical Data Analysis: Discrete Inverse Theory*, Academic, San Diego, Calif.

Menke, W. (1984b), The resolving power of cross-borehole tomography, *Geophys. Res. Lett.*, *11*(2), 105–108.

Mwenifumbo, C. J., and Q. Bristow (1999), Field evaluation of a new borehole resistivity probe using capacitive electrodes, paper presented at SAGEEP99, The Symposium on the Application of Geophysics to Engineering and Environmental Problems, Environ. and Eng. Geophys. Soc., Oakland, Calif.

Olsson, O., L. Falk, O. Forslund, L. Lundmark, and E. Sandberg (1992), Borehole radar applied to the characterization of hydraulically conductive fracture zones in crystalline rock, *Geophys. Prospect.*, *40*(2), 109–142.

Peterson, J. E. (2001), Pre-inversion corrections and analysis of radar tomographic data, *J. Environ. Eng. Geophys.*, *6*(1), 1–18.

Rector, J. W., and J. K. Washbourne (1994), Characterization of resolution and uniqueness in crosswell direct-arrival traveltime tomography using the Fourier projection slice theorem, *Geophysics*, *59*(11), 1642–1649.

Rubin, Y., G. Mavko, and J. Harris (1992), Mapping permeability in heterogeneous aquifers using hydrologic and seismic data, *Water Resour. Res.*, *28*(7), 1809–1816.

Schön, J. H. (1998), *Physical Properties of Rocks: Fundamentals and Principles of Petrophysics*, 583 pp., Pergamon, New York.

Sudicky, E. A. (1986), A natural gradient experiment on solute transport in sand aquifers: Spatial variability of hydraulic conductivity and its role in the dispersion process, *Water Resour. Res.*, *22*(13), 2069–2089.

Topp, G. C., J. L. Davis, and A. P. Annan (1980), Electromagnetic determination of soil water content: Measurements in coaxial transmission lines, *Water Resour. Res.*, *16*(3), 574–582.

Tronicke, J., N. Blindow, R. Gross, and M. A. Lange (1999), Joint application of surface electrical resistivity- and GPR-measurements for groundwater exploration on the island of Spiekeroog-northern Germany, *J. Hydrol.*, *223*(1–2), 44–53.

Tronicke, J., P. Dietrich, U. Wahlig, and E. Appel (2002a), Integrating surface georadar and crosshole radar tomography: A validation experiment in braided stream deposits, *Geophysics*, *67*(5), 1495–1504.

Tronicke, J., H. Paasche, K. Holliger, and A. G. Green (2002b), Combining crosshole georadar velocity and attenuation tomography for site characterization: A case study in an unconsolidated aquifer, in *Ninth International Conference on Ground Penetrating Radar*, edited by S. Koppenjan and H. Lee, *Proc. SPIE Int. Soc. Opt. Eng.*, *4758*, 170–175.

Valle, S., L. Zanzi, and F. Rocca (1999), Radar tomography for NDT: Comparison of techniques, *J. Appl. Geophys.*, *41*(2–3), 259–269.

Vasco, D. W., J. E. Peterson, and E. L. Majer (1996), A simultaneous inversion of seismic traveltimes and amplitudes for velocity and attenuation, *Geophysics*, *61*(6), 1738–1757.

Wharton, R. P., G. A. Hazen, R. N. Rau, and D. L. Best (1980), Advancements in electromagnetic propagation logging, *SPE Pap. 9267*, Soc. of Pet. Eng., Richardson, Tex.

Wright, D. L., T. P. Grover, K. J. Ellefsen, J. W. Lane, and P. G. Kase (1996), Radar tomography at Mirror Lake, New Hampshire: 3-D visualization and a brine tracer experiment, paper presented at Symposium on the Application of Geophysics to Environmental and Engineering Problems, Environ. and Eng. Geophys. Soc., Keystone, Colo.

Young, R. A., and Y. Sun (1996), 3D ground penetrating radar imaging of a shallow aquifer at Hill Air Force Base, Utah, *J. Environ. Eng. Geophys.*, *1*(2), 97–108.

Zhou, B., and P. K. Fullagar (2001), Delineation of sulphide ore-zones by borehole radar tomography at Hellyer Mine, Australia, *J. Appl. Geophys.*, *47*(3–4), 261–269.

W. Barrash and M. D. Knoll, Center for Geophysical Investigation of the Shallow Subsurface (CGISS), Boise State University, 1910 University Drive, Boise, ID 83725, USA.

K. Holliger and J. Tronicke, Swiss Federal Institute of Technology, Institute of Geophysics, ETH-Hönggerberg, CH-8093 Zürich, Switzerland. (jens@aug.ig.erdw.ethz.ch)